Carbon 232 (2025) 119797

Contents lists available at ScienceDirect

Carbon

journal homepage: www.elsevier.com/locate/carbon

Tailoring hydrogen adsorption *via* charge transfer at bimetallic $Cr_{0.48}Ru_{0.52}$ alloy nanoparticles decorated on carbon nanofiber for enhanced hydrogen evolution catalysis

Dasol Jin [a,1], Jiwon Kim [a,1], Ramesh Kumar Chitumalla [b,1], Yeji Yim [a], In Young Kim [a], Joonkyung Jang [b,**], Myung Hwa Kim [a,*]

[a] Department of Chemistry & Nanoscience, Ewha Womans University, Seoul, 03760, Republic of Korea
[b] Department of Nanoenergy Engineering, Pusan National University, Busan, 46241, Republic of Korea

ARTICLE INFO

Keywords:
Hydrogen adsorption
Charge transfer
Hydrogen evolution reaction
Anchoring
Hybrid carbon nanofiber

ABSTRACT

Designing and synthesizing highly efficient and stable electrocatalysts for the hydrogen evolution reaction (HER) is crucial for the practical and large-scale application of hydrogen sources. Recent research has focused on tuning the electronic structure of electrocatalysts to achieve optimal HER activity, with particular emphasis on interfacial engineering to induce electron transfer and optimize HER kinetics. In this study, as part of research into heterointerface engineering, bimetallic $Cr_{0.48}Ru_{0.52}$ alloy nanoparticles decorated on carbon nanofibers ($Cr_{0.48}Ru_{0.52}$/CNFs) were fabricated through a simple electrospinning and post-calcination process to serve as an efficient alkaline HER catalyst. The $Cr_{0.48}Ru_{0.52}$/CNFs demonstrated exceptional electrocatalytic HER performance, with an overpotential of only 13 mV at -10 mA cm^{-2} and a Tafel slope of 60.8 mV dec^{-1}, indicating high catalytic activity compared to commercial benchmark catalysts (*i.e.*, Ru/C and Pt/C). First-principles density functional theory calculations support these results, revealing that $Cr_{0.48}Ru_{0.52}$ balances proton reduction (Volmer step) and H* desorption (Tafel/Heyrovsky step) processes during electrocatalysis, as evidenced by the near-zero hydrogen adsorption (ΔG_{H^*}) value (*ca.* -0.11 eV). Therefore, this study highlights that $Cr_{0.48}Ru_{0.52}$/CNFs, with noble Ru comprising only half of the total metal content, can promote optimal HER kinetics under alkaline condition.

1. Introduction

Amidst a deepening traditional energy crisis and growing environmental concerns, there has been a consensus on promoting renewable energy sources in pursuit of sustainable development [1,2]. Among the most promising alternatives, hydrogen production has garnered significant attention as an eco-friendly energy solution, offering pollution-free and highly efficient utilization. Over the past few decades, electrochemical hydrogen production has attracted considerable interest, spurring the search for effective electroactive catalysts [3,4]. A crucial prerequisite for achieving efficient hydrogen evolution reaction (HER) is the development of catalysts with high intrinsic activity, stability, and a large specific area to facilitate fast electron transfer during the process. Platinum (Pt) is widely recognized as a key precious metal for HER catalysis, primarily due to its ability to form optimal Pt-H bonds that enhance the adsorption and reduction of H^+ ions while facilitating the release of generated H_2 [5]. However, the scarcity and high cost of precious metals have spurred extensive research into developing electrocatalysts with lower precious metal content. This has resulted in various design strategies for synthesizing hybrid frameworks that effectively integrate multiple components, such as metal precursors and polymer precursors within a carbon matrix [6–10]. Carbon-based nanomaterials have garnered significant interest as low-cost supports for active HER electrocatalysts through various approaches [11,12]. These materials are produced by incorporating electrochemically active transition metals into one- or two-dimensional carbon nanostructures, offering the potential for low-cost mass production of catalysts while reducing reliance on scarce noble metals. In the context of engineering

* Corresponding author.
** Corresponding author.
E-mail addresses: jkjang@pusan.ac.kr (J. Jang), myungkim@ewha.ac.kr (M.H. Kim).
[1] These authors contributed equally to this work.

https://doi.org/10.1016/j.carbon.2024.119797
Received 30 June 2024; Received in revised form 23 October 2024; Accepted 2 November 2024
Available online 6 November 2024

heterogeneous interfaces with a carbon matrix, electrospinning has been extensively utilized in numerous studies [13–15]. This technique involves controlling precursor conditions, such as the amount of added metal, the polymer used as the carbon matrix, and the volume of solvent; also, this approach aims to alter the electronic structure of the catalysts following post-calcination, potentially driving phase transformations within the solid solution. These reconfigurations, which range from composite states with mixed phases to fully homogenized intermetallic alloys exhibiting unique crystalline structures not observed in the individual elements, could result in shifts in the d-band position at the active sites of the newly synthesized electrocatalysts. Furthermore, these structural changes enable the study of charge density differences in electron distribution, particularly between states before and after molecule adsorption [16,17].

In electrocatalysis, as in heterogeneous catalysis, the rate of reaction is highly dependent on both the extrinsic physical properties and the intrinsic electronic structure of the electrocatalyst [18]. These factors influence reaction kinetics by controlling the adsorption of intermediate species on the surface, activation energy, and overall energy barriers. Especially, the HER is an ideal model for investigating this complexity due to its single desired product (H_2) and its important role in hydrogen-based energy conversion [19]. In this point, recently, many studies have used HER as a bridge to connect fundamental surface electrocatalysis with experimental nanoengineering and computational quantum chemistry, with the aim of developing ideal electrocatalysts.

For alkaline HER, taking the most well-studied surfaces (*i.e.*, Pt (111) [20] and Ru (0001) [21]), the Pt (111) surface has an optimal hydrogen adsorption free energy (ΔG_{H^*}) close to zero; however, its high energy barrier for water dissociation hinders its HER activity. Conversely, Ru (0001) has a low water dissociation barrier but suffers from strong hydrogen adsorption (more negative value of ΔG_{H^*}), which limits the product desorption. This trend follows the Brønsted−Evans−Polanyi (BEP) relationship, which shows that the activation energy of a process depends on the reaction enthalpy [22]. In the case of water dissociation, especially, generating adsorbed species (*e.g.*, H* and OH*) requires a low energy barrier [22,23], which necessitates strong adsorption of these species on the catalyst surface. According to d-band theory, which elucidates how the energy levels of a transition metal's d-electrons influence hydrogen adsorption, an optimal catalyst for the HER should have a d-band center that promotes moderate hydrogen binding [24,25]. Specifically, this balance is crucial: if the binding is too strong, it can impede the desorption of hydrogen, while if it is too weak, it can limit the adsorption of hydrogen. Therefore, the design of efficient alkaline HER catalysts should optimally balance water dissociation and H*/OH* adsorption abilities, aiming for appropriate H-binding and/or OH-binding energies and a low water dissociation barrier.

Herein, we systematically fabricated and investigated bimetallic $Cr_{0.48}Ru_{0.52}$ alloy nanoparticles decorated on carbon nanofiber ($Cr_{0.48}Ru_{0.52}$/CNFs) as efficient HER catalysts under alkaline condition in which the catalysts were prepared through a facile electrospinning and post-calcination process. A key aspect of our approach was the strategic use of a minimal amount of noble metal within the carbon nanofiber matrix, ensuring practicality for large-scale production and feasible application in the chemical industry. Comprehensive analyses were conducted to evaluate the physical and electrochemical properties of as-prepared hybrid nanomaterials; additionally, density functional theory (DFT) simulations were employed to gain deeper insights into the HER activity of the electrocatalysts, aiming to provide a rational explanation for their HER performances in alkaline solution.

2. Experimental

2.1. Materials

Chromium (III) chloride hexahydrate ($CrCl_3{\cdot}6H_2O$), ruthenium (III) chloride hydrate ($RuCl_3{\cdot}xH_2O$), poly(vinylpyrrolidone) (PVP, MW ≈ 1 300 000), potassium hydroxide (KOH), potassium nitrate (KNO_3), hexaammineruthenium (III) chloride ($[Ru(NH_3)_6]Cl_3$) and Nafion (5 wt% solution) were purchased from Sigma-Aldrich (St. Louis, MO, USA). Ethanol (99.9 %) was purchased from Ducksan (Korea). Commercial M/C (M = Pt and Ru; 20 wt% metal loading on Vulcan XC-72, respectively) was purchased from Fuel Cell store. All other chemicals used were of analytical grade without further purification, and all solutions used for experiments were prepared with deionized water (resistivity ≥18 MΩ cm).

2.2. Synthesis of $Cr_{0.48}Ru_{0.52}$/CNFs

$Cr_{0.48}Ru_{0.52}$/CNFs were prepared using an electrospinning and post-calcination process. 70 mg of a precursor mixture (molar ratios of $CrCl_3{\cdot}6H_2O$:$RuCl_3{\cdot}xH_2O$ = 1:1) was dissolved in 2.8 mL of a mixed solvent (ethanol:water = 1.2:1 in *v/v* ratio). Then, 300 mg of PVP was added to the metal precursor mixed solution. The mixed metal precursors/PVP solution was stirred continuously overnight to be stabilized at room temperature. The prepared solution was filled in a syringe and spouted through a syringe needle at a flow rate of 8 μL min^{-1} using an electrospinning system (NanoNC ESR200R2). For the electrospinning process, the distance between the needle of the syringe and the aluminum plate was 11 cm, and the applied voltage was 9 kV. The collected as-spun products were subjected to thermal annealing in a tube furnace, involving two steps: First, the temperature was raised to 180 °C at a heating rate of 2 °C min^{-1} and held at 180 °C for 1 h under an air-conditioned atmosphere. Second, the stabilized nanofibers were annealed at 800 °C under Ar atmosphere with a flow rate of 300 sccm and maintained at this temperature for 1 h. For comparative purpose, carbon nanofibers with single metal compositions (denoted as Cr/CNF and Ru/CNF, respectively) were synthesized using electrospinning solutions containing the corresponding metals ($CrCl_3{\cdot}6H_2O$ or $RuCl_3{\cdot}xH_2O$) under identical synthesis conditions as mentioned above.

2.3. Physical characterization

The physicochemical characterization of $Cr_{0.48}Ru_{0.52}$/CNFs were measured and characterized by inductively coupled plasma atomic emission spectroscopy (ICP-AES; Perkin-Elmer OPTIMA 8300), field emission scanning electron microscope (FE-SEM; JEOL JSM-7610F), high-resolution transmission electron microscopy (HR-TEM; JEOL JEM-ARM 200F NEOARM) with an energy dispersive X-ray spectrometer (EDS), X-ray diffraction (XRD; Rigaku D/Max-2000/PC diffractometer using Cu Kα radiation), angle-resolved X-ray photoelectron spectrometer (AR-XPS) and X-ray absorption spectroscopy (XAS). K-edge XAS spectra of samples were simultaneously collected with those of reference foils at beamline 10C of the Pohang Accelerator Laboratory, Republic of Korea.

2.4. Electrochemical characterization

For the electrochemical analysis, the synthesized electrocatalysts were dispersed in a solution comprising distilled water (2 mL), ethanol (1 mL), and 5 wt% Nafion (2 μL) at a concentration of 3 mg mL^{-1} for each catalyst. Subsequently, 4 μL of each catalyst ink was loaded onto a glassy carbon (GC) disk electrode (3 mm in diameter) and dried at 50 °C for 10 min in an oven. This loading process was repeated five times for each material, resulting in a total loading of 60 μg onto a polished GC substrate electrode. For comparison, 20 μg of commercial M/C materials (M = Ru and Pt) were also loaded onto the GC substrate, respectively. Prior to loading, the GC electrodes were polished using a polish cloth and a 0.3 μm aluminum powder slurry. All electrochemical measurements were performed in a three-electrode cell system with *i*R compensation. The catalyst-modified GC electrode served as the working electrode, while a saturated-calomel electrode (SCE) and coiled Au wire acted as the reference and counter electrodes, respectively.

Rotating disk electrode (RDE) voltammetry was conducted using an electrochemical analyzer (733D, CH Instruments, Inc.) equipped with an RDE-rotor (BASi). The measured current densities (j, mA cm^{-2}) were normalized by the geometric surface areas (GSAs) of the respective electrodes. The GSAs were determined through chronocoulometric experiments conducted in 0.1 M KNO_3 (aq) containing 10 mM hexaammineruthenium (III) chloride ($[Ru(NH_3)_6]Cl_3$).

2.5. Computational calculations

Four distinct electrocatalyst systems, namely $Cr_{0.48}Ru_{0.52}$(101), Pt (111), Ru(0001), and Cr(110), were investigated using computational calculation. Each system consisted of a periodic supercell with four layers, for a total of 64 atoms. The selection of the most stable and low-index surfaces was considered for conducting our simulations. Notably, the $Cr_{0.48}Ru_{0.52}$(101) system exhibited a 1:1 ratio of Cr and Ru atoms. The bottom two layers of the surface were held fixed, while the top two layers and the adsorbates (H_2O and H*) were allowed to relax completely during the geometry optimizations. A significant vacuum (30 Å) was introduced in the z-direction of the supercell to avoid spurious interactions between repeated slabs. Our approach involved employing spin-polarized plane-wave density functional theory (DFT) simulations with Grimme's D3 dispersion-corrected Perdew-Burke-Ernzerhof (PBE) [26] exchange-correlation functional, which incorporated the Becke-Johnson damping function [27,28]. The geometries were relaxed until the maximal energy difference was less than 10^{-5} eV and the Hellmann-Feynman force on every atom was less than 0.02 eV $Å^{-1}$. The electronic integrations for all simulations were performed using the Monkhorst-Pack scheme [29] with 1 × 1 × 1 k-points. To represent the Kohn-Sham orbitals, a plane-wave basis set with a kinetic energy cutoff of 400 eV was utilized. The projector augmented-wave (PAW) method was employed using the Vienna ab initio simulation package (VASP 6.3.2) [30–32] under periodic boundary conditions. To evaluate the free energy changes associated with H_2O and H* adsorption on the various electrocatalyst surfaces, we employed well-established methods [33–35].

3. Results and discussion

3.1. Physicochemical characterization

The field emission scanning electron microscope (FE-SEM) images presented in Fig. 1(a–d) elucidate the morphological characteristics of the as-prepared carbon nanomaterials, all of which exhibit fibrous one-dimensional (1-D) nanostructures. The $Cr_{0.48}Ru_{0.52}$/CNFs in Fig. 1(a and b), exhibited a homogeneous distribution of small nanoparticles with an average size of 30.20 nm (±7.89 nm). The particle size distribution histogram for $Cr_{0.48}Ru_{0.52}$/CNFs is presented in Fig. S1, illustrating the even dispersion of these nanoparticles across the surface of the carbon nanofibers. The Ru/CNFs (Fig. 1c), in sharp contrast, displayed highly smooth surfaces with no apparent nanoparticles on the outer surface, whereas the Cr/CNFs (Fig. 1d) exhibited discernible small nanoparticles sparsely distributed across the nanofiber surfaces. Generally, 1-D structures with specific chemical and/or physical properties can be produced using electrospinning with solution mixtures of polymers (*e.g.*, PVP) and different metal precursors (*e.g.*, $CrCl_3{\cdot}6H_2O$ and $CrCl_3{\cdot}xH_2O$) [36]. This technique embeds additives into a polymer or carbon fibre matrix, resulting in hybrid carbon materials; consequently, the electrospinning method allows for the generation of hybrid metal/carbon nanofibers with controlled and distinct morphologies, which were also confirmed in this study, as shown in SEM images (Fig. 1a–d). The relative atomic composition ratios (Cr:Ru), as determined through inductively coupled plasma atomic emission spectroscopy (ICP-AES) analysis, were observed to be 48:52 for $Cr_{0.48}Ru_{0.52}$/CNFs. This congruence with the molar ratio of the metal precursors (specifically, $CrCl_3{\cdot}6H_2O$: $RuCl_3{\cdot}xH_2O$ = 1:1) within the electrospinning solution prior to the calcination process underscores the consistency of the experimental procedure.

Fig. 1(e) presents the X-ray diffraction (XRD) spectra of as-prepared carbon nanomaterials, $Cr_{0.48}Ru_{0.52}$/CNFs, Ru/CNFs, and Cr/CNFs, respectively. All three samples exhibited broad carbon peaks at an angle of 26°, characteristic of amorphous carbon nanofibers [37]. For $Cr_{0.48}Ru_{0.52}$/CNFs, the XRD pattern predominantly displays an amorphous structure, apart from a noticeable peak at 44.1° corresponding to the (101) plane. This specific (101) plane aligns well with the XRD

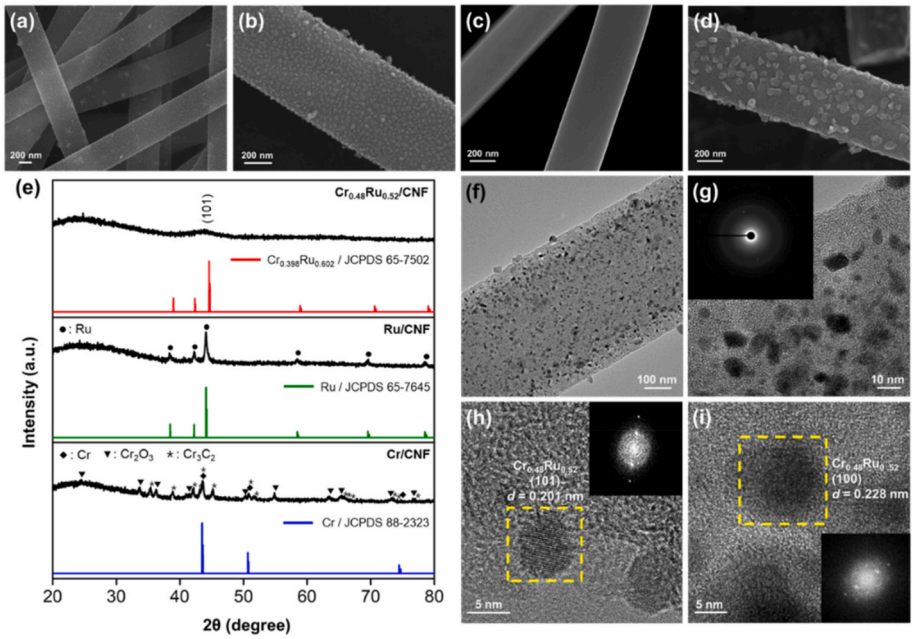

Fig. 1. SEM images of (a,b) $Cr_{0.48}Ru_{0.52}$/CNFs, (c) Ru/CNFs and (d) Cr/CNFs. (e) XRD patterns of $Cr_{0.48}Ru_{0.52}$/CNFs, Ru/CNFs and Cr/CNFs. (f,g) TEM images of $Cr_{0.48}Ru_{0.52}$/CNF along with corresponding SAED pattern (inset). (h,i) HR-TEM images of $Cr_{0.48}Ru_{0.52}$/CNF with respective FFT patterns (insets). (A colour version of this figure can be viewed online.)

pattern of hexagonal close-packed (hcp) structured $Cr_{0.398}Ru_{0.602}$ (JCPDS #65-7502), which shares a comparable atomic composition ratio with $Cr_{0.48}Ru_{0.52}$/CNFs. The presence of the (101) plane $Cr_{0.48}Ru_{0.52}$/CNFs underscores its existence within the carbon nanofiber framework. In fact, the broadening of diffraction patterns in $Cr_{0.48}Ru_{0.52}$/CNFs can be ascribed to both the overlap with the broad carbon peak and the relatively smaller particle size of the $Cr_{0.48}Ru_{0.52}$ nanoparticles [38]. In Ru/CNFs, the XRD diffraction peaks exhibit a highly crystalline lattice, consistent with the hcp-Ru (JCPDS #65-7645). On the other hand, Cr/CNFs display diverse phases in the diffraction patterns, including metallic Cr, Cr_2O_3, and Cr_3C_2. The presence of various phases in Cr/CNFs is attributed to the higher reduction potential of Cr^{3+} ions from $CrCl_3$ compared to the noble metal ion Ru^{3+} derived from $RuCl_3$ [39].

The transmission electron microscopy (TEM) analysis, along with corresponding fast Fourier transform (FFT) images, was employed to examine the crystalline domain structure of the material under investigation. The TEM image of $Cr_{0.48}Ru_{0.52}$/CNF (Fig. 1f) displays well-distributed $Cr_{0.48}Ru_{0.52}$ nanoparticles evenly dispersed across the carbon nanofibers. The selected area electron diffraction (SAED) pattern of $Cr_{0.48}Ru_{0.52}$/CNF confirms its characteristic amorphous structure (Fig. 1g), revealing a highly diffuse pattern, which is consistent with the XRD patterns (*vide supra*). However, for a more detailed analysis of the crystal domain within the bimetallic alloy decorated on carbon nanofiber, HR-TEM images in Fig. 1(h and i) revealed lattice spacings of 0.201 and 0.228 nm, respectively. These values closely correspond to the spacings between the (101) and (100) planes of the hexagonal phase in the reference $Cr_{0.398}Ru_{0.602}$ alloy (JCPDS #65-7502).

Fig. 2(a) illustrates the even distribution of the C, Cr and Ru elements throughout the entirety of the $Cr_{0.48}Ru_{0.52}$/CNF. The spatial arrangement of Cr within the carbon nanofibers containing the bimetallic alloy manifests a notably discontinuous pattern. Larger nanoparticles, in particular, tend to be predominantly localized at the exterior interface of the composite matrix. In contrast, the distribution of the Ru constituent demonstrates a distinct uniformity, extending consistently across the entire surface of the composite. The elemental mapping results, thus, serve as compelling evidence for the successful formation of hybrid nanomaterial (*i.e.*, carbon nanofiber-supported bimetallic $Cr_{0.48}Ru_{0.52}$ alloy). Fig. S2 shows a TEM-EDS elemental mapping image of Ru/CNF, demonstrating a homogeneous distribution of C and Ru across the entire nanomaterial, supporting the results mentioned above. The material features a smooth surface, with small nanoparticles embedded internally. Additionally, to further explore the morphological features at different metal ratios, a series of Cr_xRu_{1-x}/CNF samples were synthesized with varying Cr/Ru ratios, specifically $Cr_{0.33}Ru_{0.67}$/CNF and $Cr_{0.67}Ru_{0.33}$/CNF, corresponding to 1:2 and 2:1 ratio, respectively. Both

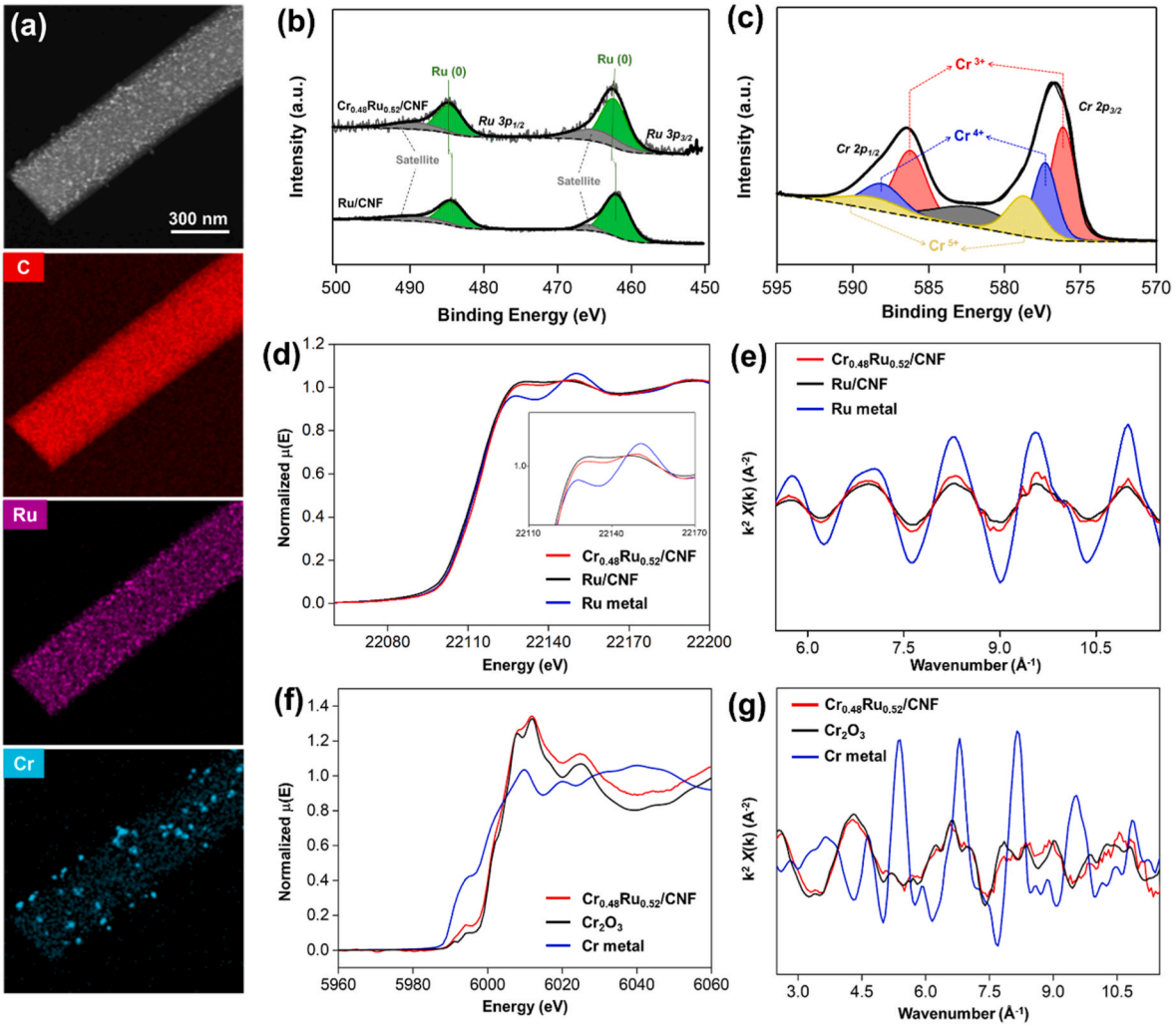

Fig. 2. (a) TEM-EDS elemental mapping of $Cr_{0.48}Ru_{0.52}$/CNF (red: C, purple: Ru, cyan: Cr). High resolution XPS spectra of $Cr_{0.48}Ru_{0.52}$/CNFs in (b) Ru 3p and (c) Cr 2p regions on the surface. Ru K-edge (d) XANES and (e) k^2-weighted EXAFS spectra of $Cr_{0.48}Ru_{0.52}$/CNFs, Ru/CNFs, and reference Ru metal. Cr K-edge (f) XANES and (g) k^2-weighted EXAFS spectra of $Cr_{0.48}Ru_{0.52}$/CNFs, Cr/CNFs, and reference Cr metal. (For interpretation of the references to colour in this figure legend, the reader is referred to the Web version of this article.)

SEM (Fig. S3) and TEM-EDS (Fig. S4) images consistently showed that nanoparticles sprouted and protruded onto the surface of the nanofibers; additionally, the particle distribution increased with higher Cr content. The XRD patterns, as shown in Fig. S5, revealed distinct crystal phases depending on the molar ratio. $Cr_{0.67}Ru_{0.33}$/CNF exhibited a phase-separated structure, presenting a mixture of Cr_2O_3 and Cr_3C_2, whereas $Cr_{0.33}Ru_{0.67}$/CNF primarily displayed a hcp-$Cr_{0.398}Ru_{0.602}$ alloy phase (JCPDS: 65-7502), with a minor presence of Cr_3C_2. In comparison with $Cr_{0.48}Ru_{0.52}$/CNF, this indicates that the formation of a bimetallic alloy is achievable under the applied synthetic conditions, which aligns with the binary Cr-Ru solid solution phase diagram [40]. In here, a key question arises regarding the role of Cr in the morphological evolution under our synthetic conditions. As shown in Fig. S6, the TEM image of the single-metal Ru/CNF exhibited a smooth surface, in contrast to the bimetallic Cr_xRu_{1-x}/CNF series ($x = 0.48$ and 0.66). With increasing Cr content, the nanoparticles became more densely distributed on the surface, accompanied by an increase in particle size. This behavior is clearly attributed to the presence of Cr, as the Ru/CNF sample showed a nearly smooth surface with encapsulated nanoparticles confined to the interior of the carbon nanofibers. The distinct morphological differences likely result from the varied thermal kinetics of Cr and Ru ions [41,42]. Cr ions, with different thermal properties, could diffuse more rapidly or react more readily with the carbon support, promoting nanoparticle growth on the surface and resulting in a rougher texture. The variations in thermal behavior between heterogeneous metal ions contribute to changes in surface roughness, leading to morphological transformations, as previously reported [43–45].

To elucidate the valence states and elemental composition of the $Cr_{0.48}Ru_{0.52}$/CNFs, X-ray photoelectron spectrometer (XPS) analysis was conducted on the prepared samples. In Fig. S7, the survey XPS spectrum of $Cr_{0.48}Ru_{0.52}$/CNFs reveals carbon as the predominant element, evident from the strong intensity of the C 1s peak. The bimetallic $Cr_{0.48}Ru_{0.52}$ nanoalloys constitute a minor fraction of the composite surface. The observed sharp C peak corresponds to graphite carbon, while the O peak signifies absorbed oxygen on the graphene surface [46]. Fig. 2(b) presents the XPS spectra of the Ru $3p_{1/2}$ and Ru $3p_{3/2}$ regions, positioned at *ca.* 484.4 and 462.2 eV, respectively, with a doublet separation of 22.8 eV; these findings are consistent with prior studies indicating a predominant metallic Ru(0) state within the entire $Cr_{0.48}Ru_{0.52}$/CNFs composite [47]. In comparison to Ru/CNFs (*i.e.*, carbon nanofiber with a single Ru-metal precursor), the Ru 3p peaks in $Cr_{0.48}Ru_{0.52}$/CNFs show a positive shift towards higher binding energy. In general, the chemical shift observed in XPS depends on the electronegativity of the atoms surrounding the metal [48]. In this case, the higher electronegativity of Ru atoms (a value of 2.2) leads to a greater attraction of electrons from the neighboring Cr atoms (a value of 1.6). In the bimetallic $Cr_{0.48}Ru_{0.52}$ alloy within the carbon nanofiber matrix, therefore, this shift could be attributed to heterogeneous bonding caused by the formation of a bimetallic alloy between electron-rich Ru and electron-deficient Cr. The Cr 2p spectra were analyzed by deconvoluting the correlated spin-orbit split peaks, as depicted in Fig. 2(c). The Cr 2p core-level XPS profiles exhibit a distinctive doublet induced by spin-orbit splitting, corresponding to the $2p_{3/2}$ and $2p_{1/2}$ states [49]. The detection of Cr in high-valence states suggests partial oxidation of metallic Cr at the near-surface region. This oxidation likely arises from a chemical shift toward higher binding energies in the transition metal orbital region, indicating electron transfer from Cr to Ru [50]. As a result, this electron transfer generates electron-rich Ru sites, which are known to demonstrate high activity for electrocatalysis. The presence of oxidized Cr species aligns with the presence of multiple peaks observed in the XRD patterns of Cr/CNFs (*vide supra*).

The X-ray absorption spectroscopy (XAS) was employed for further investigation into the valence states and local coordination structures of the $Cr_{0.48}Ru_{0.52}$/CNFs. Fig. 2(d) presents the X-ray absorption near edge structure (XANES) in the Ru K-edge region of $Cr_{0.48}Ru_{0.52}$/CNFs. Reference measurements of single Ru/CNFs and pure Ru metal in the same region are also included, with the inset displaying locally magnified diagrams for clarity. The Ru K-edge XANES spectrum revealed the electron transition behavior in Ru, spanning from 1s to 4d/4f orbitals, evident in the shoulder near the absorption threshold of Ru metal [51, 52]. The absorption energy value closely resembles that of metallic Ru, signifying a zero-valent oxidation state for $Cr_{0.48}Ru_{0.52}$/CNFs. Furthermore, the investigation of the local atomic coordination environment of Ru within $Cr_{0.48}Ru_{0.52}$/CNFs is conducted through analysis of the k^2-weighted Ru K-edge extended X-ray absorption fine structure (EXAFS) spectra, as illustrated in Fig. 2(e). The k^2-weighted EXAFS spectra of $Cr_{0.48}Ru_{0.52}$/CNFs exhibit similarities to the reference Ru metal, indicating an equivalence in the local electronic configuration of Ru, as observed in metallic Ru. The Fourier-transformed (FT) radial structures based on k^2-weighted EXAFS reveal the emergence of a Ru-Ru peak at approximately 2.4 Å in the Ru K-edge region (Fig. S8a). The structural configuration of Cr within the $Cr_{0.48}Ru_{0.52}$/CNFs was examined using Cr K-edge XANES and EXAFS, in comparison to metallic Cr and Cr_2O_3 references. As presented in Fig. 2(f), the XANES spectrum of $Cr_{0.48}Ru_{0.52}$/CNFs closely resembled that of Cr_2O_3, implying a comparable electronic configuration between Cr in $Cr_{0.48}Ru_{0.52}$/CNFs and Cr_2O_3. Similarly, the k^2-weighted EXAFS spectra of $Cr_{0.48}Ru_{0.52}$/CNFs exhibited a strong resemblance to Cr_2O_3 (Fig. 2g). In the FT-EXAFS spectra within the Cr K-edge region, a peak at 1.6 Å emerged, attributed to Cr-O coordination (Fig. S8b). This observation confirms the oxidation of Cr^{3+} occurring at the outer surface of the bimetallic alloy-embedded carbon nanofiber, where the local atomic structure closely resembles that of Cr_2O_3 [39].

3.2. Electrochemical characterization

There is no doubt about the desperate need for an efficient and resource-economizing catalyst for hydrogen production. Here, the electrocatalytic activities of as-prepared nanomaterials were investigated toward HER in an alkaline solution utilizing a three-electrode configuration system. Fig. 3(a) revealed the HER activities of $Cr_{0.48}Ru_{0.52}$/CNFs, along with Ru/CNFs, Cr/CNFs, and commercially available M/C materials (where M = Ru and Pt, both having 20 wt% metal loading on Vulcan XC-72), serving as unambiguous activity benchmarks for HER catalysts. The investigations were conducted in Ar-saturated 1 M KOH (*aq*) solution; and the polarization curves were normalized by their respective electrode geometric surface areas (GSAs) for accurate comparisons (For more detail, see *Experimental*). The superior alkaline HER catalytic performance of $Cr_{0.48}Ru_{0.52}$/CNFs was highlighted by its lowest onset potential and smallest overpotential at -10 mA cm^{-2}, outperforming commercial samples and Ru/CNFs. Note that the alkaline HER activity of Cr/CNFs was significantly deficient, resulting in the absence of a discernible HER feature within the potential range shown in Fig. 3(a). Furthermore, the fast reaction kinetics of $Cr_{0.48}Ru_{0.52}$/CNFs, contributing to its improved inherent HER activity, were validated through Tafel plots (η *vs.* log *j*, where η represents overpotential, and *j* is the GSA-normalized current density) derived from the measured polarization curves (Fig. 3b) [53]. The smaller Tafel slope of $Cr_{0.48}Ru_{0.52}$/CNFs (60.8 mV dec^{-1}) indicated a more facile HER process, implying that the catalyst-modified electrode required a low overpotential to enhance the current density. In comparison, Ru/CNFs (65.4 mV dec^{-1}) and commercial samples (63.4 mV dec^{-1} for Pt/C and 75.9 mV dec^{-1} for Ru/C) exhibited less favorable electron transfer at the catalytic interface. For a comprehensive evaluation of the electrocatalytic HER performance, the mass activities of the catalysts were calculated (Fig. 3c). The mass activities were determined by normalizing the current values with the actual amount of noble metal in the nanomaterials loaded onto the working electrode. Among the tested catalysts, $Cr_{0.48}Ru_{0.52}$/CNFs displayed the highest mass activity (423.9 mA mg^{-1}), followed by Pt/C (312.1 mA mg^{-1}) and Ru/C (149.5 mA mg^{-1}). This indicates that the bimetallic alloy-decorated carbon nanofiber of $Cr_{0.48}Ru_{0.52}$/CNFs is capable of generating high current densities for

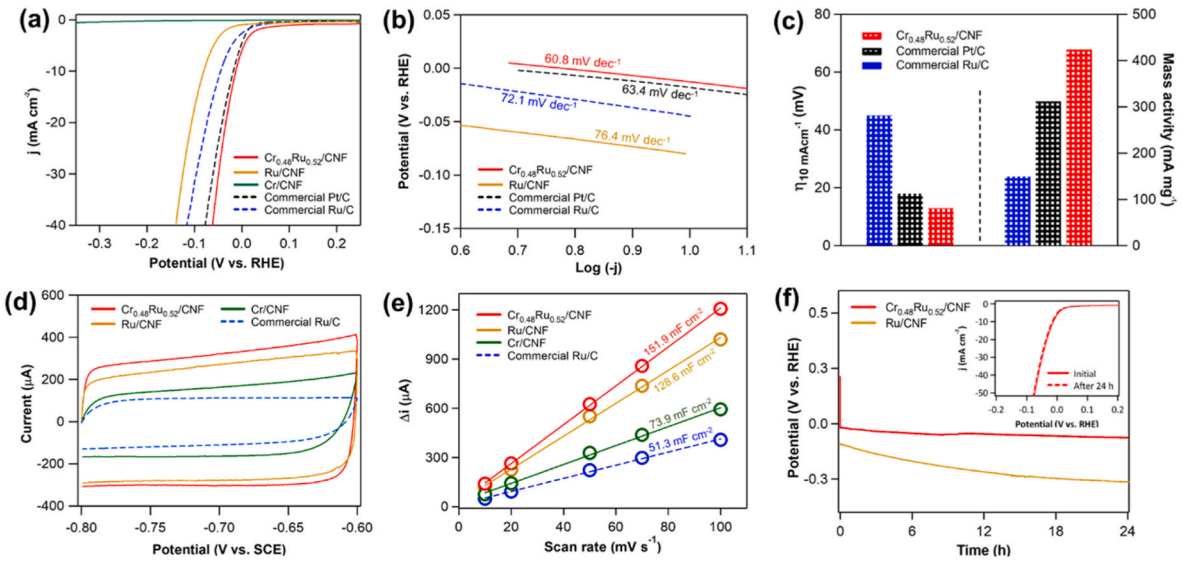

Fig. 3. Electrochemical HER performances. (a) *i*R-compensated polarization curves of as-prepared nanomaterials in 1 M KOH (*aq*) with a rotating rate of 1600 rpm and a scan rate of 10 mV s^{-1}. (b) Tafel plots derived from LSV curves in (a). (c) Comparison of overpotentials at −10 mA cm^{-2} (left) and mass activities at an overpotential of 50 mV (right). (d) Cyclic voltammograms of nanomaterials in 1 M KOH (*aq*) at a scan rate of 50 mV s^{-1} with a potential range of 0.2 V. (e) Plots of absolute charging/discharge current density (Δ*i*) at −0.7 V (*vs.* SCE) against scan rate. The corresponding C_{dl} (mF cm^{-2}) values were normalized to geometric surface area. (f) Chronopotentiometric plots of $Cr_{0.48}Ru_{0.52}$/CNFs and single Ru/CNFs at −10 mA cm^{-2} for 24-h in 1 M KOH (*aq*). Inset: LSV curves before and after 24-h of continuous HER performance related to Fig. 3(f). (A colour version of this figure can be viewed online.)

HER even with a small amount of noble metals. To make a precise comparison, we compared the reaction descriptors (*i.e.*, measured potentials achieving −10 mA cm^{-2} and Tafel slopes) of $Cr_{0.48}Ru_{0.52}$/CNFs with other Ru-based electrocatalysts recently reported in the literature (Table 1). Remarkably, our carbon-based nanomaterial with a low precious metal concentration exhibited catalytic activities comparable to the other catalysts documented in prior studies.

Carbon-based electrode materials have gained considerable attention in the pursuit of high-performance electrochemical double layer capacitors due to their substantial accessible surface area, enabling efficient interactions with the electrolyte, and their excellent electrical conductivity [60,61]. In this study, we estimated the electrochemically active surface area (ECSA) of the prepared electrode materials using double layer capacitance (C_{dl}) measurements during the charging and discharging processes. In order to evaluate the electrochemical properties of the catalysts, cyclic voltammetry (CV) was performed in 1 M KOH (*aq*) within a non-faradaic potential range. Fig. S9 shows the CV curves for as-prepared carbon nanomaterials with various scan rates of 10, 20, 50, 75, 100 mV s^{-1} in a range of −0.8 ~ −0.6 V (*vs.* SCE). All the catalysts exhibited rapid charging and discharging patterns, similar to general rectangular cyclic voltammograms. In addition, the respective CVs for each carbon nanomaterial were compared at a scan rate of 50 mV s^{-1} for the same potential range as shown in Fig. 3(d); in contrast to the tested samples, $Cr_{0.48}Ru_{0.52}$/CNFs exhibited notably rapid charging/discharging shapes, while sustaining a high current. Based on the CV curves, the absolute difference values (Δ*i*) between the cathodic and anodic currents at the midpoint of the potential region displayed a linear relationship ($R^2 > 0.996$) with the potential scan rate, as shown in Fig. 3 (e). The slopes of Δ*i vs.* scan rate increased in the following order: $Cr_{0.48}Ru_{0.52}$/CNFs (151.9 mF cm^{-2}) > Ru/CNFs (128.6 mF cm^{-2}) > Cr/CNFs (73.9 mF cm^{-2}) > Ru/C (51.3 mF cm^{-2}). These capacitive current values are considered indicative of the ECSAs of the electrode materials, closely related to the actual number of active sites for electrode reactions. Specifically, $Cr_{0.48}Ru_{0.52}$/CNFs demonstrated the largest ECSA, reflecting the advantageous characteristics of the bimetallic alloy composition. The durability of catalysts represents a crucial complementary parameter in the context of industrial applications, even when the materials exhibit promising catalytic activity. In this study, the stability of $Cr_{0.48}Ru_{0.52}$/CNFs was evaluated during continuous hydrogen production; this investigation involved monitoring potential shifts at −10 mA cm^{-2} for ongoing hydrogen evolution in 1 M KOH (*aq*), utilizing chronopotentiometric technique (Fig. 3f). Notably, $Cr_{0.48}Ru_{0.52}$/CNFs demonstrated a negligible potential shift during 24-h operation, indicating excellent stability. Additionally, there was also no significant difference in the LSV polarization curves before and after a 24-h HER for $Cr_{0.48}Ru_{0.52}$/CNFs (inset of Fig. 3f). In contrast, the potential of single Ru/CNFs gradually declined due to the challenging conditions of the HER process, underscoring the beneficial contribution of the Cr component in the bimetallic $Cr_{0.48}Ru_{0.52}$ alloy-decorated carbon nanofiber, which enhances long-term stability. Given that $Cr_{0.48}Ru_{0.52}$/CNF is a one-dimensional catalyst prepared through electrospinning, influenced by metal precursors and polymers, alkali resistance tests were conducted, as illustrated in Fig. S10. Even under harsh alkaline conditions using a corrosive electrolyte (1 M NaOH (*aq*) with 1 M NaCl) at high temperature (60 °C), the $Cr_{0.48}Ru_{0.52}$/CNF catalyst maintained its original shape without any deterioration, indicating its robust durability.

Table 1
Comparison of the alkaline HER activities of various Ru-based electrocatalysts in the literature.

Solution	Catalyst	Tafel slope (mV dec^{-1})	Overpotential at −10 mA cm^{-2} (mV)	Reference
1 M KOH	$Cr_{0.48}Ru_{0.52}$/CNFs	60.8	13	This work
	RuO_2@CNT@MOF	61.6	13	[54]
	Fe_3O_4/RuO_2-C	68	94	[55]
	Co@RuCo-3	50	46	[56]
	Ru-Cu_2O/CF	50	31	[57]
	Co-xRu@NG-500	23.4	30	[58]
	RuNi-20NF	–	21	[59]

3.3. Theoretical calculations

To provide additional validation for our experimental results and to explore the heightened HER activity of the $Cr_{0.48}Ru_{0.52}$/CNFs compared to the other electrocatalysts employed in this investigation, first-

principles quantum mechanical simulations were performed. Considering that the electrochemical reduction of an H_2O molecule into an adsorbed hydrogen atom (Volmer step) on the electrocatalyst surface is a crucial and kinetic limiting stage in the HER process [62], examination was conducted on the adsorption of H_2O over the four electrocatalysts (*vide supra*) as well as the associated alterations in adsorption free energy. The H_2O molecule was adsorbed on the surfaces of $Cr_{0.48}Ru_{0.52}$(101), Pt(111), Ru(0001), and Cr(110), and their geometries were optimized at various adsorption sites to determine the most thermodynamically stable configurations, as depicted in Fig. 4. The adsorbed H_2O molecule adopted a horizontal orientation with a height of approximately 2.20 Å from the surface, and the ∠H–O–H angle was approximately 105.5°. On the $Cr_{0.48}Ru_{0.52}$ surface, the H_2O molecule was adsorbed at the Ru and Cr sites to identify the most effective catalytic reaction site.

As depicted in Fig. 5(a), the calculated adsorption free energies of H_2O at the Ru and Cr sites of $Cr_{0.48}Ru_{0.52}$ (−0.695 eV and −0.585 eV) are more negative than that of Pt (−0.465 eV). The more negative adsorption free energy of H_2O on $Cr_{0.48}Ru_{0.52}$ reveals the strong interaction between H_2O and the electrocatalyst, which facilitates the O–H bond dissociation [63]. However, the electrocatalyst's HER performance cannot be correlated only to its adsorption free energy of H_2O. Additionally, the adsorption free energy of H* is a very important parameter for assessing the HER performance of the electrocatalyst. Considering that d-band theory explains how the energy levels of a transition metal's d-electrons influence hydrogen adsorption, our DFT calculations presented in Fig. 5(a) are crucial for understanding the energetics of reaction intermediates. This insight is a key component of the micro-kinetic analysis conducted for the alkaline HER mechanism. The H-binding strength is quantified in terms of the free energy change associated with the hydrogen adsorption (ΔG_{H^*}) on the electrocatalyst surface. A moderate ΔG_{H^*} value ($\Delta G_{H^*} \approx 0.0$ eV) will lead to efficient HER by the electrocatalyst. On the other hand, more positive or more negative ΔG_{H^*} values lead to poor HER performance [64,65]. As shown in Fig. 5(b), the calculated ΔG_{H^*} value of the $Cr_{0.48}Ru_{0.52}$ (−0.11 eV) is closest to 0.0 eV than those of the other three electrocatalysts. The near-zero ΔG_{H^*} value of the $Cr_{0.48}Ru_{0.52}$ balances the proton reduction (Volmer step) and H* desorption (Tafel/Heyrovsky step) processes, making it an efficient electrocatalyst for the HER [62]. The ΔG_{H^*} value of the Pt(111) is −0.18 eV, which is comparable to that of $Cr_{0.48}Ru_{0.52}$(101). However, the larger ΔG_{H^*} values (−0.35 and −0.54 eV, respectively) of Ru(0001) and Cr(110) lead to slower HER kinetics.

Furthermore, charge density difference (CDD) plots were generated to comprehend the direction of charge transfer at the interface between H_2O and the electrocatalyst. The CDD plots (Fig. 5c–f) reveal that electrons are transferred from the H_2O molecule to the surfaces of the electrocatalysts. The cyan region around H_2O indicates charge depletion, while the yellow region on the surfaces shows charge accumulation. Bader's quantum theory of atoms in molecules [66], along with the software developed by the Henkelman group [67], was employed to estimate the charge transferred from H_2O to the $Cr_{0.48}Ru_{0.52}$ and Pt surfaces. Bader charge analysis demonstrates that $Cr_{0.48}Ru_{0.52}$ receives significantly more charge from H_2O than Pt. The estimated charge transfer from H_2O to $Cr_{0.48}Ru_{0.52}$ is 0.13 |e|, while Pt only receives 0.09 |e|. The substantial charge transfer to $Cr_{0.48}Ru_{0.52}$ facilitates easier O–H bond dissociation, resulting in more efficient H_2 evolution than Pt. In summary, the results of the first-principles quantum mechanical simulations suggest that $Cr_{0.48}Ru_{0.52}$ is a promising electrocatalyst for the HER compared to the other electrocatalysts. These theoretical findings are consistent with our experimental HER activity result.

4. Conclusions

In summary, the investigation of ΔG_{H^*} values for the as-prepared hybrid metal/carbon nanomaterials revealed that optimizing the electrocatalytic sites for water dissociation can synergistically improve the multi-step reactions involved in the alkaline HER. This was demonstrated through the synthesis of $Cr_{0.48}Ru_{0.52}$/CNFs using a simple electrospinning and post-calcination process, in which the catalysts showed the optimum HER activity with an ultralow overpotential of 13 mV to achieve a current density of −10 mA cm^{-2} and a Tafel slope of 60.8 mV dec^{-1}, as well as long-term durability of up to 24-h. This performance surpasses that of most previously reported HER catalysts. Moreover, the micro-kinetics analysis, supported by DFT calculations, confirms lower energy barriers for H_2O dissociation and a faster alkaline HER process. This work, therefore, not only underscores the guiding role of *d*-band theory, but also presents a straightforward strategy for developing highly efficient alkaline HER electrocatalyst.

CRediT authorship contribution statement

Dasol Jin: Writing – review & editing, Writing – original draft, Visualization, Validation, Methodology, Investigation, Formal analysis, Data curation, Conceptualization. **Jiwon Kim:** Visualization, Methodology, Investigation, Formal analysis, Data curation, Conceptualization. **Ramesh Kumar Chitumalla:** Writing – original draft, Visualization, Software, Investigation, Formal analysis, Data curation. **Yeji Yim:** Visualization, Writing – review & editing. **In Young Kim:** Validation, Resources. **Joonkyung Jang:** Supervision, Software, Resources, Project administration, Funding acquisition. **Myung Hwa Kim:** Supervision, Resources, Project administration, Funding acquisition, Conceptualization.

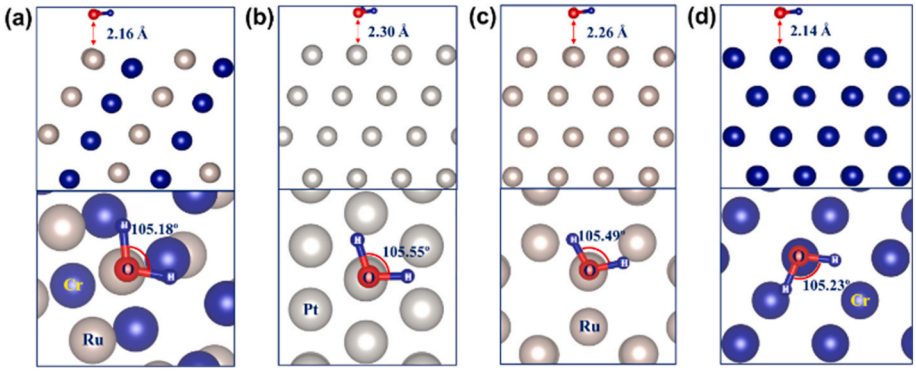

Fig. 4. Optimized geometries of H_2O adsorbed (a) $Cr_{0.48}Ru_{0.52}$(101), (b) Pt(111), (c) Ru(0001), and (d) Cr(110) systems, respectively, and their important geometric parameters calculated at the rPBE level of theory. The top and bottom panels show the side and top views, respectively. (A colour version of this figure can be viewed online.)

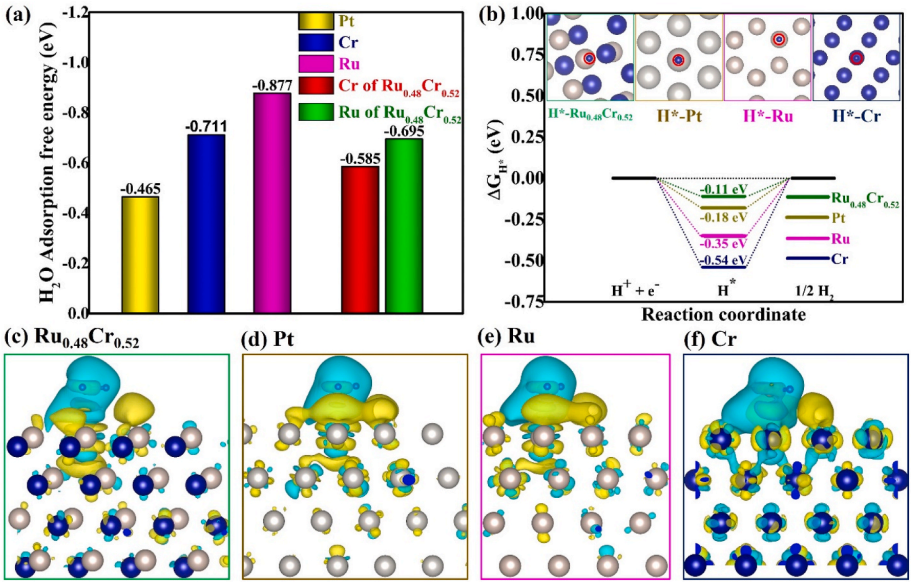

Fig. 5. (a) Adsorption free energies of H_2O on Pt(111), Cr(110), Ru(0001), and $Cr_{0.48}Ru_{0.52}$(101) and (b) calculated hydrogen adsorption free energies (ΔG_{H^*}) on $Cr_{0.48}Ru_{0.52}$(101), Pt(111), Ru(0001), and Cr(110) surfaces. (c–f) Charge density difference plots of H_2O-adsorbed electrocatalyst systems. The cyan region around H_2O represents a charge depletion (positive charge) and the yellow region on the surface represents a charge accumulation (negative charge), plotted with an isovalue of 0.0025 $e^-/Å^{-3}$. (For interpretation of the references to colour in this figure legend, the reader is referred to the Web version of this article.)

Data availability

The authors declare that the experimental data and relevant analysis of this work are available from the corresponding authors (MHK and JJ) upon reasonable request.

Declaration of competing interest

The authors declare that they have no known competing financial interests or personal relationships that could have appeared to influence the work reported in this paper.

Acknowledgements

This work was financially supported by the National Research Foundation of Korea (NRF) funded by the Ministry of Science and ICT or by the Ministry of Education (NRF-2018R1A6A1A03025340 and RS-2023-00252880 for MHK), and funded by the Korea government (MSIT) (RS-2023-00220748 for JJ). JJ acknowledges the support by the Korea Planning & Evaluation Institute of Industrial Technology and fund by the Korean government (Ministry of Trade, Industry, and Energy, Ministry of Science and ICT, Ministry of the Interior and Safety, National Fire Agency, Project Title: Development of gas hydrate extinguishing agent and fire suppression technology for inaccessible fires, Project Number: 2760000002). IYK appreciates the support of the Pohang Accelerator Laboratory (2023-1st-10C-091) for XAS study in this work.

Appendix A. Supplementary data

Supplementary data to this article can be found online at https://doi.org/10.1016/j.carbon.2024.119797.

References

[1] Q. Hu, K. Gao, X. Wang, H. Zheng, J. Cao, L. Mi, Q. Huo, H. Yang, J. Liu, C. He, Nat. Commun. 13 (2022) 3958.
[2] R. Andaveh, G. Barati Darband, M. Maleki, A. Sabour Rouhaghdam, J. Mater. Chem. A 10 (2022) 5147–5173.
[3] M. Lao, P. Li, Y. Jiang, H. Pan, S.X. Dou, W. Sun, Nano Energy 98 (2022) 107231.
[4] G. Li, T. Sun, H.-J. Niu, Y. Yan, T. Liu, S. Jiang, Q. Yang, W. Zhou, L. Guo, Adv. Funct. Mater. 33 (2023) 2212514.
[5] Y. Zhao, P.V. Kumar, X. Tan, X. Lu, X. Zhu, J. Jiang, J. Pan, S. Xi, H.Y. Yang, Z. Ma, T. Wan, D. Chu, W. Jiang, S.C. Smith, R. Amal, Z. Han, X. Lu, Nat. Commun. 13 (2022) 2430.
[6] L. Gao, Z. Yang, T. Sun, X. Tan, W. Lai, M. Li, J. Kim, Y.-F. Lu, S.-I. Choi, W. Zhang, C. Ma, S.C. Smith, Y.-G. Zhou, H. Huang, Adv. Energy Mater. 12 (2022) 2103943.
[7] W. Yang, P. Cheng, Z. Li, Y. Lin, M. Li, J. Zi, H. Shi, G. Li, Z. Lian, H. Li, Adv. Funct. Mater. 32 (2022) 2205920.
[8] Y. Zhang, Y. Zhang, B. Tian, H. Li, Z. Zeng, D. Ho, Mater. Today Energy 29 (2022) 101133.
[9] Y. Tan, J. Feng, H. Dong, L. Liu, S. Zhao, F. Lai, T. Liu, Y. Bai, I.P. Parkin, G. He, Adv. Funct. Mater. 33 (2023) 2209967.
[10] B. Wang, F. Yang, L. Feng, Small 19 (2023) 2302866.
[11] Y. Qiu, J. Liu, M. Sun, J. Yang, J. Liu, X. Zhang, X. Liu, L. Zhang, Chin. J. Struct. Chem. 41 (2022) 2207040.
[12] X. Zhao, J. Wang, J. Kang, X. Wang, H. Yu, C.-F. Du, Chin. J. Struct. Chem. 42 (2023) 100159.
[13] W. Li, L. Zhao, C. Wang, X. Lu, W. Chen, ACS Appl. Mater. Interfaces 13 (2021) 46998–47009.
[14] R. Qi, L. Zhang, S. Ren, B. Shi, M. Zhong, Z.-J. Chen, X. Lu, Nano Lett. 24 (2024) 8964–8972.
[15] T. Gong, J. Zhang, Y. Liu, L. Hou, J. Deng, C. Yuan, Chem. Eng. J. 451 (2023) 139025.
[16] S.T. Finn, J.E. Macdonald, ACS Appl. Mater. Interfaces 8 (2016) 25185–25192.
[17] Y. Yang, Y. Yu, J. Li, Q. Chen, Y. Du, P. Rao, R. Li, C. Jia, Z. Kang, P. Deng, Y. Shen, X. Tian, Nano-Micro Lett. 13 (2021) 160.
[18] Y. Zheng, Y. Jiao, A. Vasileff, S.-Z. Qiao, Angew. Chem. Int. Ed. 57 (2018) 7568–7579.
[19] Y. Zheng, Y. Jiao, M. Jaroniec, S.-Z. Qiao, Angew. Chem. Int. Ed. 54 (2015) 52–65.
[20] I. Ledezma-Yanez, W.D.Z. Wallace, P. Sebastián-Pascual, V. Climent, J.M. Feliu, M.T.M. Koper, Nat. Energy 2 (2017) 17031.
[21] Y. Zheng, Y. Jiao, Y. Zhu, L.H. Li, Y. Han, Y. Chen, M. Jaroniec, S.-Z. Qiao, J. Am. Chem. Soc. 138 (2016) 16174–16181.
[22] J.L. Fajin, M.N.D.S. Cordeiro, J.R. Gomes, J. Phys. Chem. A 118 (2014) 5832–5840.
[23] C. Li, H. Gao, W. Wan, T. Mueller, Phys. Chem. Chem. Phys. 21 (2019) 24489–24498.
[24] C. Fan, Y.-A. Zhu, M.-L. Yang, Z.-J. Sui, X.-G. Zhou, D. Chen, Ind. Eng. Chem. Res. 54 (2015) 5901–5913.
[25] M.T. Tang, X. Liu, Y. Ji, J.K. Norskov, K. Chan, J. Phys. Chem. C 124 (2020) 28083–28092.
[26] J.P. Perdew, K. Burke, M. Ernzerhof, Phys. Rev. Lett. 77 (1996) 3865–3868.
[27] A.D. Becke, E.R. Johnson, J. Chem. Phys. 123 (2005) 154101.
[28] S. Grimme, S. Ehrlich, L. Goerigk, J. Comput. Chem. 32 (2011) 1456–1465.
[29] H.J. Monkhorst, J.D. Pack, Phys. Rev. B Solid State 13 (1976) 5188–5192.
[30] G. Kresse, J. Furthmüller, Phys. Rev. B 54 (1996) 11169–11186.
[31] G. Kresse, J. Furthmüller, Comput. Mater. Sci. 6 (1996) 15–50.
[32] G. Kresse, J. Hafner, Phys. Rev. B 48 (1993) 13115–13118.
[33] J.-Y.Y. Zhang, T. He, M. Wang, R. Qi, Y. Yan, Z. Dong, H. Liu, H. Wang, B.Y. Xia, Nano Energy 60 (2019) 894–902.
[34] D. Li, Z. Li, R. Zou, G. Shi, Y. Huang, W. Yang, W. Yang, C. Liu, X. Peng, Appl. Catal. B Environ. 307 (2022) 121170.

[35] B.S. Singu, R.K. Chitumalla, D. Mandal, Y. Kim, G.H. Kim, H.T. Chung, J. Jang, H. Kim, Appl. Catal. B Environ. 328 (2023) 122421.
[36] L. Xiao, Y. Wang, T. Fu, Q. Liu, F. Guo, Y. Zhang, M. Li, X. Bo, T. Liu, J. Colloid Interface Sci. 654 (2024) 150–163.
[37] L. Dong, G. Wang, X. Li, D. Xiong, B. Yan, B. Chen, D. Li, Y. Cui, RSC Adv. 6 (2016) 4193–4199.
[38] C.F. Holder, R.E. Schaak, ACS Nano 13 (2019) 7359–7365.
[39] D. Jin, Y. Lee, I.Y. Kim, C. Lee, M.H. Kim, J. Mater. Chem. A 11 (2023) 16243–16254.
[40] L.A. Cornish, R. Süss, A. Watson, S.N. Prins, Plat, Metals Rev 51 (2007) 104–115.
[41] J. Łuczak, M. Kroczewska, M. Baluk, J. Sowik, P. Mazierski, A. Zaleska-Medynska, Adv. Colloid Interface Sci. 314 (2023) 102864.
[42] T. Rodenas, I. Luz, G. Prieto, B. Seoane, H. Miro, A. Corma, F. Kapteijn, F.X. Llabrés I Xamena, J. Gascon, Nat. Mater. 14 (2015) 48–55.
[43] L. Huang, N. Wang, M. Qi, Z. Liu, Z. Xu, Q. Zhang, Z. Shu, S. Shan, Y. Bian, J. Chen, Y. Jiao, Int. J. Hydrogen Energy 88 (2024) 1217–1225.
[44] S. Amirpoor, A. Dolati, Int. J. Hydrogen Energy 84 (2024) 14–27.
[45] W. Zhang, Y. Wang, T. Fang, X. Tang, Z. Ding, Y. Han, R. Guo, P. Qi, X. Liu, Chem. Eng. J. 498 (2024) 155449.
[46] J. Kang, T. Kwon, S. Shin, H. Oh, Y. Lee, M.H. Kim, J. Alloys Compd. 965 (2023) 171318.
[47] W. Li, Y. Zhao, Y. Liu, M. Sun, G.I.N. Waterhouse, B. Huang, K. Zhang, T. Zhang, S. Lu, Angew. Chem., Int. Ed. 60 (2021) 3290–3298.
[48] T. Kwon, A. Yu, S.-J. Kim, M.H. Kim, C. Lee, Y. Lee, Appl. Surf. Sci. 563 (2021) 150293.
[49] S. Ge, R. Xie, B. Huang, Z. Zhang, H. Liu, X. Kang, S. Hu, S. Li, Y. Luo, Q. Yu, J. Wang, G. Chai, L. Guan, H.-M. Cheng, B. Liu, Energy Environ. Sci. 16 (2023) 3734–3742.
[50] X. Wang, J. Zhang, Z. Wang, Z. Lin, S. Shen, W. Zhong, Chin J. Struc, Chem 42 (2023) 100035.
[51] Y. Lin, Z. Tian, L. Zhang, J. Ma, Z. Jiang, B.J. Deibert, R. Ge, L. Chen, Nat. Commun. 10 (2019) 162.
[52] T.-Y. Chen, G.-W. Lee, Y.-T. Liu, Y.-F. Liao, C.-C. Huang, D.-S. Lin, T.-L. Lin, J. Mater. Chem. A 3 (2015) 1518–1529.
[53] F. Bao, E. Kemppainen, I. Dorbandt, R. Bors, F. Xi, R. Schlatmann, R. van de Krol, S. Calnan, Chemelectrochem 8 (2021) 195–208.
[54] Y. Xu, C. Yang, Q. Deng, Y. Zhou, C. Mao, Y. Song, M. Zhu, Y. Zhang, Appl. Surf. Sci. 612 (2023) 155870.
[55] A. Shekhawat, R. Samanta, S. Barman, ACS Appl. Energy Mater. 5 (2022) 6059–6069.
[56] H. Huang, H. Jung, C.-Y. Park, S. Kim, A. Lee, H. Jun, J. Choi, J.W. Han, J. Lee, Appl. Catal. B Environ. 315 (2022) 121554.
[57] P. Shen, B. Zhou, Z. Chen, W. Xiao, Y. Fu, J. Wan, Z. Wu, L. Wang, Appl. Catal. B Environ. 325 (2023) 122305.
[58] Y. Xia, Z.-Q. Li, H. Sun, C. Zhang, T. Fujita, Z.-X. Cai, J. Colloid Interface Sci. 662 (2024) 995–1004.
[59] X. Mao, Z. Liu, C. Lin, J. Li, P.-K. Shen, Inorg. Chem. Front. 10 (2023) 558–566.
[60] S. Yu, M. Liu, Q. Wang, J. Xu, Y. Zou, C. Xiang, F. Xu, L. Sun, M. Jiang, Z. Hu, J. Alloys Compd. 937 (2023) 168316.
[61] R. Ding, Y. Chen, X. Li, Z. Rui, K. Hua, Y. Wu, X. Duan, X. Wang, J. Li, J. Liu, Small 18 (2022) 2105335.
[62] Q. Mo, W. Zhang, L. He, X. Yu, Q. Gao, Appl. Catal. B Environ. 244 (2019) 620–627.
[63] K. Xu, H. Cheng, H. Lv, J. Wang, L. Liu, S. Liu, X. Wu, W. Chu, C. Wu, Y. Xie, Adv. Mater. 30 (2018) 1703322.
[64] X. Liu, K. Ni, C. Niu, R. Guo, W. Xi, Z. Wang, J. Meng, J. Li, Y. Zhu, P. Wu, Q. Li, J. Luo, X. Wu, L. Mai, ACS Catal. 9 (2019) 2275–2285.
[65] H. Wu, W. Xiao, C. Guan, X. Liu, W. Zang, H. Zhang, J. Ding, Y.P. Feng, S. J. Pennycook, J. Wang, Nano Energy 48 (2018) 73–80.
[66] R.F.W. Bader, Chem. Rev. 91 (1991) 893–928.
[67] G. Henkelman, A. Arnaldsson, H. Jonsson, Comput. Mater. Sci. 36 (2006) 354–360.